PHYSICAL REVIEW FLUIDS **1**, 053201 (2016)

Reduced-dimension model of liquid plug propagation in tubes

Hideki Fujioka*
Center for Computational Science, Tulane University, New Orleans, Louisiana 70118, USA

David Halpern†
Department of Mathematics, University of Alabama, Tuscaloosa, Alabama 35487, USA

Jason Ryans‡ and Donald P. Gaver, III§
Department of Biomedical Engineering, Tulane University, New Orleans, Louisiana 70118, USA
(Received 17 February 2016; published 6 September 2016)

We investigate the flow resistance caused by the propagation of a liquid plug in a liquid-lined tube and propose a simple semiempirical formula for the flow resistance as a function of the plug length, the capillary number, and the precursor film thickness. These formulas are based on computational investigations of three key contributors to the plug resistance: the front meniscus, the plug core, and the rear meniscus. We show that the nondimensional flow resistance in the front meniscus varies as a function of the capillary number and the precursor film thickness. For a fixed capillary number, the flow resistance increases with decreasing precursor film thickness. The flow in the core region is modeled as Poiseuille flow and the flow resistance is a linear function of the plug length. For the rear meniscus, the flow resistance increases monotonically with decreasing capillary number. We investigate the maximum mechanical stress behavior at the wall, such as the wall pressure gradient, the wall shear stress, and the wall shear stress gradient, and propose empirical formulas for the maximum stresses in each region. These wall mechanical stresses vary as a function of the capillary number: For semi-infinite fingers of air propagating through pulmonary airways, the epithelial cell damage correlates with the pressure gradient. However, for shorter plugs the front meniscus may provide substantial mechanical stresses that could modulate this behavior and provide a major cause of cell injury when liquid plugs propagate in pulmonary airways. Finally, we propose that the reduced-dimension models developed herein may be of importance for the creation of large-scale models of interfacial flows in pulmonary networks, where full computational fluid dynamics calculations are untenable.

DOI: 10.1103/PhysRevFluids.1.053201

I. INTRODUCTION

Liquid-lined airways exist in the lung and the instability of this lining fluid is physiologically significant and related to many pathophysiological states [1]. This instability, also known as the Plateau-Rayleigh instability [2], is induced by surface tension and may result in the formation of a liquid plug if the liquid volume exceeds a certain critical value [3]. This is a major problem in air-conducting tubes because the flow resistance due to the propagation of liquid plugs is much higher than air flow. For example, the lining liquid in a pulmonary bronchiole may form plugs that block gas exchange. Furthermore, mechanical stresses induced by moving liquid plugs may damage the pulmonary epithelium [4–6]. These phenomena are especially significant for patients suffering

*fuji@tulane.edu
†dhalpern@ua.edu
‡jryans@tulane.edu
§dpg@tulane.edu

from acute lung injury (ALI) who are sustained with mechanical ventilation. This is because the propagation of liquid plugs exacerbates the existing lung injury and can induce ventilator-induced lung injury [4,7–13]. Despite recent advances in ventilation protocols, the mortality rate for ALI remains very high at 30%–40% [14,15], with approximately 75 000 deaths annually in the US alone [16,17].

In order to predict appropriate ventilation settings, it would be desirable to estimate the motion and distribution of liquid plugs in the lung during mechanical ventilation. If successful, this could help to identify improved clinical methods for the treatment of ALI. This is a formidable task, as the pulmonary system consists of a large number of branching flexible tubes that are lined with liquid that may become unstable and form liquid plugs. To complete this type of model, it is important to understand the overall flow resistance across the network as well as the transport of liquid within the system. Unfortunately, the direct numerical simulation of multiphase flows within a large bifurcating network system of compliant tubes is computationally intractable. However, models of plugs within discrete airways using analytical methods and computational fluid dynamics (CFD) provide exceptional insight into subcomponents from which one can base full-scale models.

Original insight into the physics of plug behavior was derived by analogy to the work of Taylor [18], who investigated bubble propagation in a tube experimentally. Subsequently, Bretherton [19] derived a model to describe a Taylor bubble using lubrication theory, which showed that the liquid film thickness deposited from a progressing meniscus is $O(\mathrm{Ca}^{2/3})$ and the pressure drop across either the front or rear menisci is a function of $\mathrm{Ca}^{2/3}$ at small Ca. Here Ca is the capillary number, the ratio of viscous to surface tension forces. As pointed out by Klaseboer *et al.* [20], Bretherton's asymptotic formula for the deposited film thickness is only accurate for very small Ca. There is a 10% error for $\mathrm{Ca} = 0.005$, which increases with Ca. At large Ca, the film thickness is weakly dependent on Ca. Using scaling arguments, Aussillous and Quere [21] came with up an empirical formula for the film thickness that agreed with their experimental results up to $\mathrm{Ca} = 2$. Inspired by [21], Klaseboer *et al.* [20] derived an *ad hoc* model that more accurately describes the pressure at the bubble tip at moderate Ca. Their formula for the film thickness reduces to Bretherton's expression in the limit as $\mathrm{Ca} \to 0$ and agrees well with experimental data at large Ca. Computationally, the bubble dynamics relevant to plug flow has been investigated for a large range of Ca [22–26], for finite Reynolds number [27], and in the presence of surfactant [28–33].

More recently, plug flow was modeled analytically by Howell *et al.* [34], who analyzed the propagation of a liquid plug in a liquid-lined flexible tube in the asymptotic limit of $\mathrm{Ca} \to 0$. They showed that increasing the precursor film thickness and the wall compliance made a tube reopen more readily. However, their model did not include the contribution of the viscous drag to the pressure drop across the plug and assumed constant surface tension. Waters and Grotberg [35] expanded upon this work by considering the effect of a surfactant, which is present in the liquid lining of the lung. Computational simulations have been conducted in Refs. [36–41], which solved the Navier-Stokes equation numerically; the effect of gravity was investigated in Refs. [38,42]; non-Newtonian effects were analyzed numerically in Ref. [43]; and plug-splitting models at a single bifurcation were investigated in Refs. [44,45].

These results provide insight into plug behavior that can be used to develop a reduced-dimension understanding that can form the foundation for simulations that elucidate interactions of plugs in more complex geometries, as demonstrated by Smith and Gaver [46]. In the lung, such models were proposed by Filoche *et al.* [47], who investigated the delivery of a single bolus of the surfactant into the lung using a reduced-dimension model. However, in order to simulate interactions of multiple plugs, it is necessary to develop a more complete understanding of plug resistances and fluid balances. Furthermore, the mechanical stress field is of particular importance to the lung.

In order to develop high-resolution reduced-dimension models of plugs, we hypothesize that a plug propagating in a tube can be divided into three interrelated components (Fig. 1).

(i) The front meniscus. This region, which accumulates fluid from the precursor film of thickness h_f, was thoroughly investigated in Ref. [26].

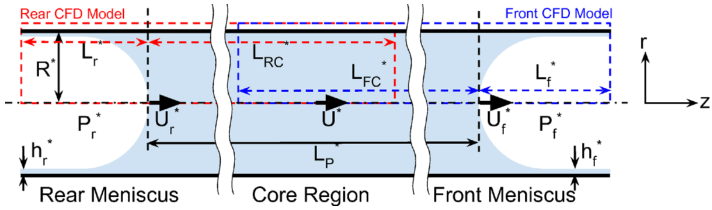

FIG. 1. A positve pressure drop $P_r^* - P_f^*$ drives a liquid plug through a cylindrical tube of radius R^*. Ahead of the plug, the tube is coated with a liquid lining of thickness h_f^*, while behind it a lining of thickness h_r^* is deposited.

(ii) The core region. The resistance in this region can be well approximated by the Poiseuille law if the plug is long enough to neglect the interaction between the front and rear menisci.

(iii) The rear meniscus. The rear meniscus of a liquid plug provides an additional pressure drop, which is equivalent to the pressure drop at the tip of a propagating finger of air in a viscous fluid [18,19]. This portion deposits a film of thickness h_r.

The three regions interact in a time-dependent manner. For example, the precursor film thickness h_f is an independent parameter and the trailing film h_r is a function of the physical properties of the system and propagation velocity. By conservation of mass, the plugs will grow or diminish in time based upon the state of the system and this will lead to changes in the plug resistance behavior.

Each of the three components have physical characteristics related to stress, flow, and fluid balances that are physiologically significant. In Sec. II we formulate these components based upon theoretical models. In Sec. III we test and improve the predictions using computational simulation. Together, these approaches provide algebraic relationships for key properties related to plug motion. In Sec. IV D we combine these components and compare these reduced-dimension predictions with the high performance computer simulations conducted in Ref. [40]. This validates the accuracy of the simplified model from a fundamental standpoint, which then provides a tool that can be faithfully used in agent-based simulations to predict flows and plug propagation behavior in highly complicated systems. In Appendixes A and B a straightforward example is finally provided so that the reader can best understand how to implement the strategy proposed herein.

II. MODEL

We consider the propagation of an axisymmetric liquid plug in a circular tube of radius R^* as described in Fig. 1. The pressure difference between front and rear air phases drives the liquid plug of viscosity μ^*. The averaged velocity in the middle cross section of the plug is defined as U^*. A thin liquid film coats the inner surface of tube. The film thickness is h_f^* in front of the plug and h_r^* in the rear of the plug. The surface tension acts at the air-liquid interface.

A. Flow resistance across a liquid plug

The flow resistance across a liquid plug in a tube is defined as

$$\Delta P^* = S_{\text{plug}}^* Q^*, \tag{1}$$

where $\Delta P^* = P_r^* - P_f^*$ is the pressure drop across the plug, Q^* is the liquid flow rate at the middle cross section of the plug, and S_{plug}^* is the plug flow resistance. We neglect the interaction between the front and rear menisci in order to apply the resistance model to a wide range of plug lengths.

We divide a liquid plug into three regions, which are the front meniscus, the rear meniscus, and the core region, which enables us to consider the resistance for each region separately,

$$S_{\text{plug}}^* = S_f^* + S_r^* + S_c^*. \tag{2}$$

We nondimensionalize the flow rate, pressure drop, and plug resistance as follows:

$$Q = Q^*/\pi R^{*2} U^*,$$
$$\Delta P = \Delta P^*/(\mu^* U^*/R^*),$$
$$S_{\text{plug}} = S^*_{\text{plug}}/(\mu^*/\pi R^{*3}),$$

where U^* is the cross-sectional averaged velocity ($U^* = Q^*/\pi R^{*2}$, i.e., $Q = 1$). Note that unstarred variables are dimensionless quantities.

In Secs. II B–II D the empirical formulas derived by Chebbi [48] based on the lubrication approximation model of Bretherton [19] are provided and our computational model is described in Sec. III. We compare these two models and discuss them in Sec. IV.

B. Rear meniscus

Bretherton [19] developed a model to describe the steady motion of a Taylor bubble [18] using lubrication theory. He derived a third-order differential equation for the film thickness in a thin region between the film and the bubble cap,

$$\frac{d^3\eta}{d\xi^3} = \frac{\eta - 1}{\eta}, \tag{3}$$

where $\eta = h^*/h^*_r$, $z^* = h^*_r(3\text{Ca}_r)^{-1/3}\xi$, and h^*_r is the constant thickness in the film region. Here $\text{Ca}_r = \mu^* U^*_r/\sigma^*$ is the rear capillary number and U^*_r is the axial (z) component of velocity at the meniscus tip, so $U^*_r = Q^*/[\pi(R^{*^2} - h^*_r)^2]$. The boundary conditions are $\eta \to 1$ as $\xi \to -\infty$, the film region, and $\frac{d^2\eta}{d\xi^2} \to P$, where P is a constant, as $\xi \to \infty$, since $\eta \gg 1$ in the bubble cap region. The latter, together with Eq. (3), implies that η is a quadratic polynomial in ξ,

$$\eta = \tfrac{1}{2}P(\xi - \xi_0)^2 + K \tag{4}$$

as $\xi \to \infty$ [20]. Here P, K, and ξ_0 are constants, which are determined by solving Eq. (3) numerically. Initial conditions for (3) come from linearizing this equation about $\eta = 1$ and then solving it over a large domain so that $\eta_{\xi\xi}(\xi = \xi_{\max})$ is approximately constant. The constant curvature of the parabolic profile in the cap region is matched with that of a spherical cap filling the tube to yield the well-known expression for the trailing film thickness, namely,

$$h_r = \frac{h^*_r}{R^*} = 1.34\text{Ca}_r^{2/3}. \tag{5}$$

in the limit $\text{Ca}_r \to 0$ [19]. Klaseboer *et al.* [20] extended the Bretherton model to include a more accurate description of the bubble tip curvature at moderate capillary numbers and derived the following expression for h_r:

$$h_r = \frac{P(3\text{Ca})^{2/3}}{1 + 2.79P(3\text{Ca})^{2/3}}, \tag{6}$$

where $P \approx 0.643$. We will use an analogous formula developed in Ref. [21] for comparison with the full computational model described below.

The pressure jump across the front meniscus of a long bubble, which is equivalent to the rear meniscus of a liquid plug, is of interest to us, since from it we can compute the flow resistance. This is defined as

$$S_r = 2 \times 1.79 \times 3^{2/3}\text{Ca}_r^{-1/3}. \tag{7}$$

More details concerning the resistance formula that we use can be found in Appendix A.

TABLE I. Coefficients of the function f_2 that appears in Eq. (8).

k	C_k
0	−0.149
1	2.04
2	0.570
3	0.233
4	0.0640
5	0.00689

C. Front meniscus

Kalliadasis and Chang [49], and later Chebbi [48], asymptotically analyzed the motion of an advancing gas-liquid interface in a cylindrical tube, which is equivalent to the front meniscus of liquid plugs. The film thickness in the front meniscus satisfies the same third-order differential equation (3) as at the rear, with some minor changes in the definitions of η and ξ. However, the boundary conditions towards the film and bubble cap regions at $\pm\infty$ are switched, with $\eta \to 1$ as $\xi \to \infty$, and $\frac{d^2\eta}{d\xi^2} \to P_f$ as $\xi \to -\infty$, where P_f is a constant. As pointed out in Ref. [19], the shape of the front meniscus is uniquely determined provided the film thickness h_f is prescribed. Both Kalliadasis and Chang [49] and Chebbi [48] were interested in determining the dependence of the apparent contact angle that the meniscus forms with the surface of the tube on the capillary number and the ratio of the precursor film thickness to the tube radius. They also examined the effect of van der Waals forces, which can become significant at very low Ca.

Of interest to us is the flow resistance of the advancing meniscus, which can be determined from the pressure drop across the interface. We define it as

$$S_f = -2 \times 3^{2/3} f_2 \mathrm{Ca}_f^{-1/3}, \tag{8}$$

where $\mathrm{Ca}_f = \mu^* U_f^*/\sigma^*$ is the capillary number, with U_f^* the axial (z) component of velocity at the front meniscus tip, which is equivalent to the cross-sectional averaged air velocity $U_f^* = Q^*/\pi(R^{*^2} - h_f^*)^2$. More details can be found in Appendix A. The function f_2 that appears in the expression for the resistance comes from a relationship for the apparent contact angle given in Ref. [48], which is inspired by the asymptotic analysis of [49]. It is given by

$$f_2(x) \simeq \sum_{k=0}^{5} C_k (\log_{10} x)^k, \tag{9}$$

where the coefficients C_k are determined numerically by using a lubrication approximation analysis similar to that given in Ref. [48]. Note this is an empirically fitted function of $x = h_f/(3\mathrm{Ca}_f)^{2/3}$, where $h_f = h_f^*/R^*$ is the nondimensional precursor liquid film thickness. Since we need f_2 to be applicable for a wide range of $h_f/(3\mathrm{Ca}_f)^{2/3}$, we generated six coefficients, while the original [48] provided four coefficients. Table I gives the coefficients C_k for $0 \leqslant k \leqslant 5$.

D. Core region

We assume that the flow in a plug core is fully developed so that we can use the Poiseuille law for the pressure drop across the plug ΔP_c^*,

$$\Delta P_c^* = \frac{8\mu^* L_P^* Q^*}{\pi R^{*4}}, \tag{10}$$

where L_P^* is the plug length. The dimensionless flow resistance is

$$S_c = 8L_P, \tag{11}$$

where $L_P = L_P^*/R^*$.

III. COMPUTATIONAL MODELS

In this section we describe the computational fluid dynamics methods used to calculate the flow resistance of the front meniscus and rear meniscus models. We assume here steady axisymmetric motion.

A. Front meniscus model

For the front meniscus computational model, we consider an air finger retracting in a liquid-filled circular tube with a constant speed U_f^*. The enclosed region labeled "Front CFD Model" in Fig. 1 schematically describes the computational domain in a moving frame with velocity U_f^*. The air phase is assumed to be inviscid and the pressure P_f is constant, which is unknown. The film thickness h_f is prescribed and the nondimensional velocity at the right end is $\mathbf{u} = (-1,0)$, which is also the velocity at the wall in the moving frame of reference. At the left end the flow is assumed to be fully developed Poiseuille flow with a uniform reference pressure $p = 0$ to include the core region.

B. Rear meniscus model

The enclosed region labeled "Rear CFD Model" in Fig. 1 schematically describes the computational domain, where an air finger propagates in a liquid-filled circular tube with a constant speed U_r^*. The liquid phase is modeled in a moving frame with speed U_r^*. The air phase is also assumed to be inviscid, with the pressure being an unknown constant P_r. The film thickness h_r is also unknown and is part of the solution. At the left end, the nondimensional velocity is $\mathbf{u} = (-1,0)$, which, as above, is also the velocity at the tube wall. At the right end, where the flow is fully developed Poiseuille flow, a uniform reference pressure $p = 0$ is applied.

C. Governing equations for front and rear meniscus models

In a frame of reference moving with constant velocity, the Stokes and continuity equations that describe the flow inside the liquid phase are

$$\nabla p = \nabla^2 \mathbf{u} \tag{12}$$

and

$$\nabla \cdot \mathbf{u} = 0, \tag{13}$$

where $p = p^*/(\mu^* U_{\rm tip}^*/R^*)$, $\mathbf{u} = \mathbf{u}^*/U_{\rm tip}^*$, and the reference velocity $U_{\rm tip}^*$ is the meniscus tip speed $U_{\rm tip}^* = U_f^*$ or U_r^*. A constant surface tension acts on the air-liquid interfaces, so the stress boundary condition is

$$-p\mathbf{n} + [(\nabla \mathbf{u}) + (\nabla \mathbf{u})^T]\mathbf{n} = -P_a\mathbf{n} + \kappa \mathrm{Ca}^{-1}\mathbf{n}, \tag{14}$$

where $\mathbf{n}$ is unit normal, P_a is the pressure of air, $P_a = P_f$ or P_r, and $\kappa = \kappa^* R^*$ is the curvature of the surface. The kinematic boundary condition on the interface is $\mathbf{u} \cdot \mathbf{n} = 0$. As mentioned earlier, the no-slip condition on the tube wall in the moving frame requires $\mathbf{u} = (-1,0)$ at $r = 1$. The steady propagation of the front and rear menisci of a liquid plug in the Stokes flow regime were computed using the numerical approach that is described in Refs. [36,40]. Once the velocity, pressure, and geometry of the plug have been determined, wall stresses and hence the resistance to flow can be ascertained.

D. Estimation of flow resistance

As stated in Sec. II A, we consider the flow resistance in each region separately. To compute the drag force, the wall shear stress is required, which, in dimensional form, is defined as

$$\tau^* = -\mu^* \frac{\partial u_z^*}{\partial r^*}. \tag{15}$$

Note that for a plug, $\tau^* \to 0$ as $z^* \to \pm\infty$ in the stationary thin film regions. In steady state, the total drag force has to balance the pressure drop across a liquid plug, so

$$2\pi R^* \int_{-\infty}^{\infty} \tau^* dz^* = \pi R^{*2} \Delta P^*, \tag{16}$$

where the right-hand side of Eq. (16) is written as the sum of three resistances

$$\pi R^{*2} \Delta P^* = \pi R^{*2} S_{\text{plug}}^* Q^* = \pi R^{*2} (S_r^* + S_f^* + S_c^*) Q^*. \tag{17}$$

The nondimensional drag force $D = D^*/\pi\mu^* U_{\text{tip}}^* R^*$ is

$$D = 2\int_{-\infty}^{\infty} \tau\, dz = \frac{U^*}{U_{\text{tip}}^*}(S_r + S_f + S_c)Q, \tag{18}$$

where $U_{\text{tip}}^* = U_f^*$ or U_r^*. Since the flow rates in the front and rear air phases and in the plug core match, we must have $Q^* = \pi R^{*2} U^* = \pi(R^* - h_r^*)^2 U_r^* = \pi(R^* - h_f^*)^2 U_f^*$ so that

$$\frac{U^*}{U_{\text{tip}}^*} = (1-h)^2, \tag{19}$$

where $h = h_f$ or h_r.

From the front meniscus model (Sec. III A), the drag force can be described by the resistances due to the front and core regions. Placing the meniscus tip at $z = 0$,

$$D_f = 2\int_{-L_{FC}}^{L_f} \tau\, dz = (1-h_f)^2 (S_f + S_c) Q. \tag{20}$$

As discussed above, we assume Poiseuille flow in the entire core region and apply the Poiseuille law for S_c. Therefore, the resistance due to the front meniscus is given by

$$S_f = \frac{D_f}{(1-h_f)^2} - 8L_P. \tag{21}$$

Note that $Q = 1$ and $S_c = 8L_P$. From the rear meniscus model (Sec. III B), the resistance in the rear meniscus is similarly computed, with Eqs. (20) and (21) replaced by

$$D_r = 2\int_{-L_r}^{L_{RC}} \tau\, dz = (1-h_r)^2 (S_r + S_c) Q \tag{22}$$

and

$$S_r = \frac{D_r}{(1-h_r)^2} - 8L_P. \tag{23}$$

IV. RESULTS AND DISCUSSION

In order to demonstrate the accuracy of our computational model, Table II compares the surface curvature at the meniscus tip of the rear part of a Taylor bubble obtained from our model with the boundary element results of Martinez and Udell [50] and the finite-element results of Giavedoni and Saita [26]. In order to achieve this comparison, we performed the rear meniscus simulations at each Ca given in Table II and obtained the bubble shape and the film thickness h_r. Then we carried

TABLE II. Surface curvature at the meniscus tip compared with other studies.

Ca	Ref. [50]	Ref. [26]	This work
0.025	1.821	1.818	1.815
0.05	1.703	1.726	1.720
0.075	1.622	1.655	1.650
0.1	1.577	1.596	1.589
0.2	1.388	1.409	1.405
0.25	1.332	1.328	1.324
0.5	0.9545	0.945	0.956
0.75	0.5207	0.545	0.587
1.0	0.1084	0.117	0.211
1.5	−0.710	−0.800	−0.723

out the front meniscus simulation prescribing $h_f = h_r(\mathrm{Ca})$. Our results agreed well with the other two studies except for $\mathrm{Ca} = 1.0$, where the curvature is close to zero and the surface is almost flat. Physiological values of the capillary number are much smaller than one and thus this approximation is appropriate.

A. Front meniscus

Figure 2(a) shows the nondimensional liquid thickness with the precursor film thickness $h_f = 0.05$ for various Ca_f. The meniscus tip is placed at $z = 0$ and $r = 0$. Near the tip, for $z < 0.8$, the surface shape is not too dependent on Ca_f when Ca_f is $O(10^{-3})$. However, for $\mathrm{Ca}_f > 1 \times 10^{-2}$ the interfacial profiles become steeper, implying smaller curvatures around the center line. This figure also shows the presence of a capillary wave in the film region whose amplitude and wavelength increase as Ca_f decreases. For $\mathrm{Ca}_f = 5 \times 10^{-1}$, this oscillation is imperceptible.

Figure 2(b) shows the nondimensional wall shear stress. Like the film thickness, the wall shear stress is a damped sinusoidal wave in the film region, whose amplitude and wavelength increase as Ca_f decreases. A local negative (positive) peak in wall shear stress appears at the point where the film thickness is locally a minimum (maximum). For all cases a local positive peak appears in the meniscus region and asymptotically approaches the Poiseuille flow value of $\tau = 4(1 - h_f)^2$ as $z \to -1$.

The velocity vector field and pressure profile in the capillary wave region shown in Fig. 3 explain the oscillating variation of shear stress. At the point where the film thickness is smallest, the velocity at the film surface is faster than at the wall to conserve the flow rate in the film region where $h = h_f$. The wall shear rate attains a large negative value and thus τ has a negative peak in this region. The large pressure gradient in this region accelerates the flow in the film towards the meniscus. In the region where the film thickness is thicker than h_f, the velocity at the film surface is slower than the velocity at the wall and therefore the wall shear rate has a positive peak here.

Since Eq. (8) is based on the approximation of $h_f \ll 1$, we cannot compare the computational S_f calculated from Eq. (21) with Eq. (8) directly because we focus on the range $0.01 \leqslant h_f \leqslant 0.12$ that is not small enough. Instead, we compute $\hat{S}_f$ from the formula

$$S_f = \hat{S}_f (1 - h_f)^{-2} \tag{24}$$

and compare with Eq. (8), which is now modified as

$$\hat{S}_f = -2 \times 3^{2/3} \tilde{f}_2 \mathrm{Ca}_f^{-1/3}. \tag{25}$$

Figure 4 shows the computational results of $\hat{S}_f/(-2 \times 3^{2/3}\mathrm{Ca}_f^{-1/3})$ versus $h_f/(3\mathrm{Ca}_f)^{2/3}$, where $\hat{S}_f/(-2 \times 3^{2/3}\mathrm{Ca}_f^{-1/3})$ corresponds to the function f_2 defined by Eq. (9). The solid line represents

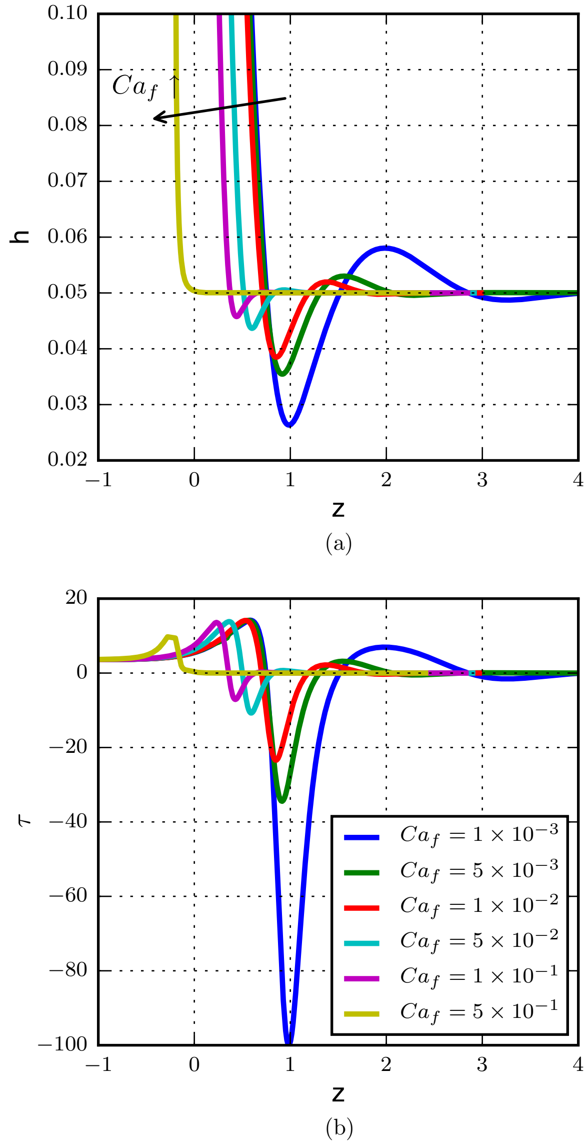

FIG. 2. Influence of the capillary number Ca_f on (a) the film thickness h and (b) the shear stress on the wall τ in the front meniscus region. Here the precursor film thickness is $h_f = 0.05$.

Eq. (9), which is a fitted polynomial with six coefficients given in Table I. The computational results agree well with Eq. (9) for large $h_f/(3\mathrm{Ca}_f)^{2/3}$ but deviate as $h_f/(3\mathrm{Ca}_f)^{2/3}$ decreases. The difference at fixed $h_f/(3\mathrm{Ca}_f)^{2/3}$ increases with h_f. Thus, a new function $\tilde{f}_2$ is proposed by adding a correction term to Eq. (9) so that

$$\tilde{f}_2(x,h_f) = f_2(x) + \frac{A h_f^m x^n}{1 + B x^n}, \tag{26}$$

where $x = h_f/(3\mathrm{Ca}_f)^{2/3}$. The constants $A = 1.02$, $B = 0.0778$, $m = 0.348$, and $n = -0.594$ were obtained using a least-squares minimization method (from the open-source PYTHON package [51]). This new function $\tilde{f}_2$ yields more accurate results than the original f_2.

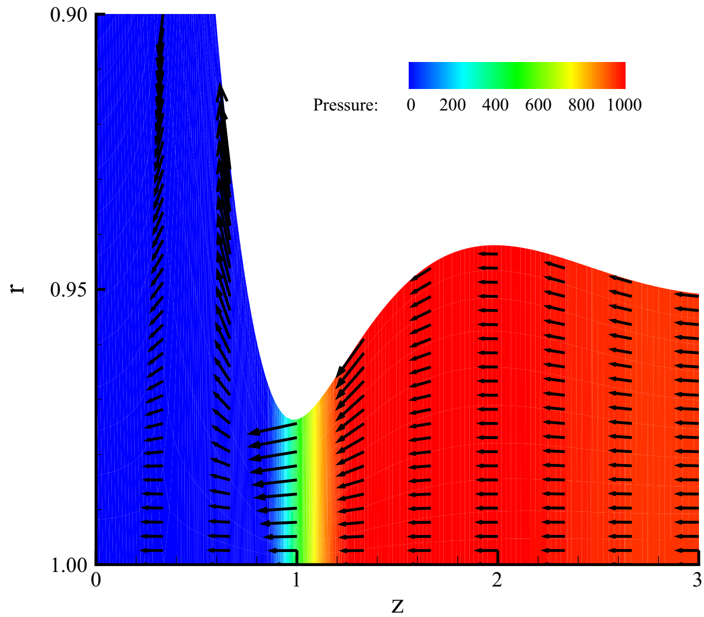

FIG. 3. Velocity and pressure profiles for $\mathrm{Ca}_f = 0.01$ for $h_f = 0.05$.

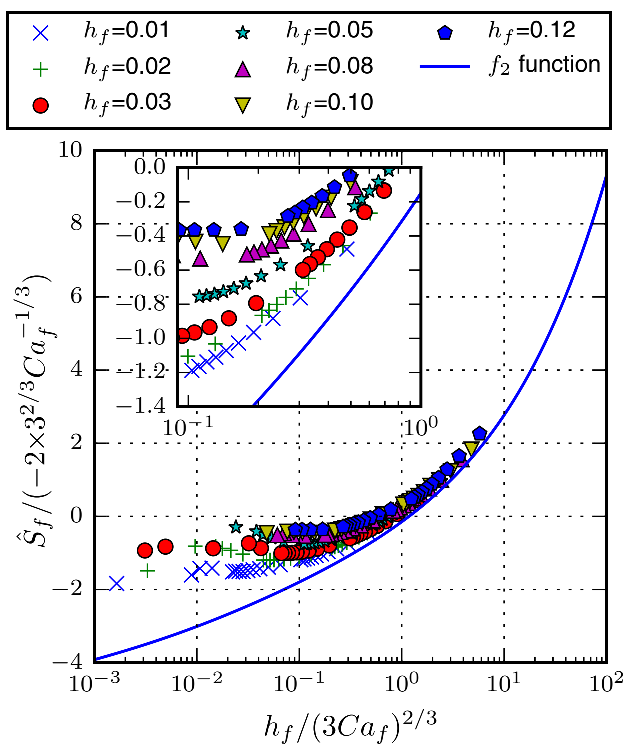

FIG. 4. Front meniscus resistance comparison between the computational results and the asymptotic formula (8) that uses the empirical function f_2 given by Eq. (9).

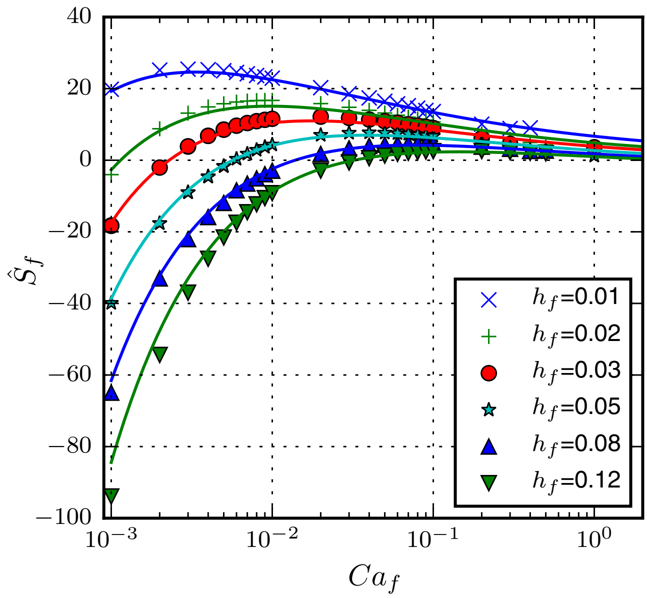

FIG. 5. Front meniscus resistance comparison between the asymptotic formula (8) that uses the modified $\tilde{f}_2$ given by Eq. (26) and the computational results. The coefficient of determination $r^2 = 0.994$.

The computational $\hat{S}_f$ and the fitted curves of Eqs. (25) and (26) are shown in Fig. 5. Here $\hat{S}_f$ becomes negative for smaller Ca_f and larger h_f. This is a result of the negative wall shear stress where the film thickness has a local minimum as shown in Fig. 2. This negative peak becomes more significant as h_f increases and dominates the drag force within the front meniscus region. The negative resistance is balanced by the positive resistance from the rear (see below) and thus the total resistance is positive.

B. Rear meniscus

The trailing film thickness of a liquid plug corresponds to the film thickness in the central region of a Taylor bubble, which is primarily a function of Ca. Bretherton [19] showed that the film thickness is expressed by Eq. (5) in the limit of $\mathrm{Ca} \to 0$. Figure 6 illustrates how the film thickness h_r of the rear meniscus model varies with Ca_r. Note that the solid line is Eq. (5) and the dashed line is the equation

$$h_r = \frac{1.34\mathrm{Ca}_r^{2/3}}{1 + 1.34 \times 2.5\mathrm{Ca}_r^{2/3}}, \tag{27}$$

which is a fitted curve of Taylor' s results proposed by Aussillous and Quere [21] and is similar to the one derived in Ref. [20] [Eq. (6)] using an extended lubrication theory approach. The computational results agree well with Eq. (27).

Similarly to the front resistance estimation, we keep the $(1 - h_r)^{-2}$ term in S_r as

$$S_r = \hat{S}_r(1 - h_r)^{-2}. \tag{28}$$

Figure 7 shows how the resistance in the rear meniscus $\hat{S}_r$ varies with Ca_f, where $\hat{S}_r$ was calculated with Eqs. (23) and (28). The solid line is plotted using Eq. (7) based on Bretherton' s analysis. For $\mathrm{Ca}_r \to 0$, $\hat{S}_r$ should approach Eq. (7). For large Ca_r, since h_r plateaus to a constant independent of

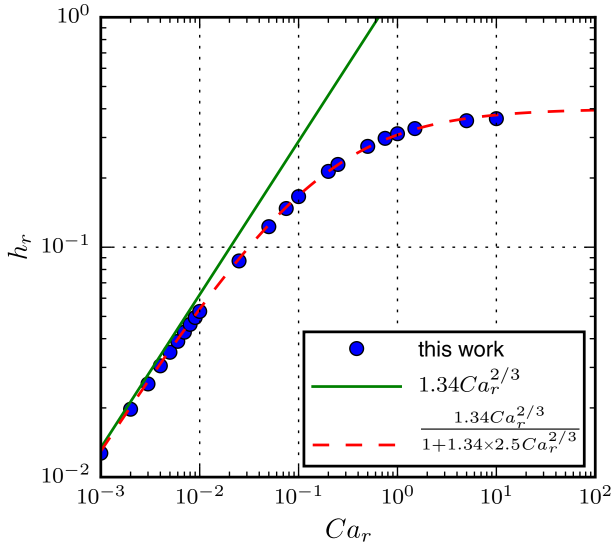

FIG. 6. Dependence of the trailing film thickness h_r on Ca_r. Note that the asymptotic formula from Bretherton's lubrication approximation [19], shown as the straight line in the log-log plot, is only good for $\mathrm{Ca} \ll 1$, while the empirical formula due to [21] is quite accurate over a large range of Ca. The coefficient of determination is $r^2 = 0.999$ from [21].

Ca_r, S_r should asymptotically approach a constant. Thus, we define the expression for $\hat{S}_r$ based on Eq. (7) as

$$\hat{S}_r = \frac{2 \times 1.79 \times 2^{2/3}\mathrm{Ca}_r^{-1/3}}{1 + A\mathrm{Ca}_r^{1/3}} + S_{r0} \tag{29}$$

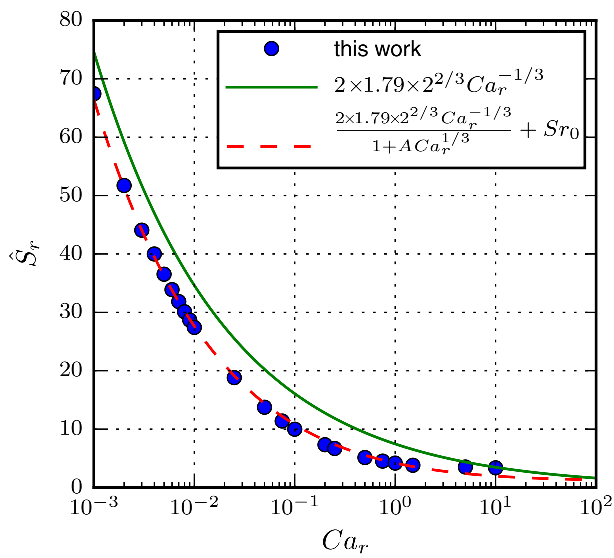

FIG. 7. Rear meniscus resistance comparison between the asymptotic formula (7), the modified resistance formula (29), and the computational results. Here $r^2 = 0.999$.

and obtained $A = 1.41$ and $S_{r0} = 1.10$ by a least-squares minimization method. This empirical correlation is displayed as the dashed line in Fig. 7 and is in much better agreement with the CFD results.

C. Overall plug flow resistance

It is well known that surface tension can have a destabilizing effect on a thin liquid layer coating the inner surface of a tube. Using a normal mode analysis, it can be shown that a small-amplitude sinusoidal disturbance with a dimensionless wavelength $l_\lambda^*/R^* = 2^{3/2}\pi$ grows most rapidly [2]. As the film thickens, a plug may form if the film thickness approximately exceeds 12% of the tube radius $h = 0.12$ [3]. We can estimate that the typical plug length created by the capillary instability is approximately $L_P = 1.36$ by using the most dangerous dimensionless wavelength $l_\lambda^*/R^* = 2^{3/2}\pi$ and the critical dimensionless film thickness of 0.12, with all fluid collected in a plug.

Thus, by applying Eq. (11), the flow resistance in the plug core region is $S_c \simeq 11$. From Fig. 7 it can be observed that for $\mathrm{Ca} < 10^{-1}$, the flow resistance in the rear meniscus (S_r) is larger than S_c. When a plug is newly created due to the capillary instability, the film thickness left on both sides can be very thin and consequently the flow resistance in the front meniscus (S_f) is very large. Therefore, the overall plug resistance is dominated by S_f and S_r until the plug length becomes very small. At that point, the dynamics in the core region become important and may not be accurately modeled using Poiseuille flow.

If a plug is instilled in or enters a tube lined with a thick liquid layer, it is possible that the flow resistance in the front meniscus (S_f) becomes negative for small Ca_f, as Fig. 5 demonstrates. However, in this situation, the front meniscus accelerates, Ca_f thus increases, and S_f changes sign and becomes positive. Since the front meniscus propagates faster than the rear, the volume of the plug must grow.

D. Comparison with CFD results

Here we validate the reduced-dimension plug flow resistance model by comparison to CFD results of plug propagation [40], where the full Navier-Stokes equations were computed for the entire liquid phase using the finite volume method with a body-fit mesh. In order to compare the time-dependent CFD results to the reduced-dimension plug resistance model, we integrate the equation of motion for a liquid plug given by

$$\frac{d(m^*U^*)}{dt^*} = \pi R^{*2}(\Delta P^* - S^*_{\mathrm{plug}} Q^*), \tag{30}$$

where $m^* = \rho^* V^*$ is the mass of a plug, V^* is the plug volume, and ρ^* is the density of the liquid. The resistance of a plug S^*_{plug} is computed using Eq. (2), which is the sum of the resistances with contributions from the front meniscus [Eqs. (24)–(26)], the rear meniscus [Eqs. (28) and (29)], and the plug core region [Eq. (11)]. The plug volume changes due to differences between front and rear film thicknesses and the speeds of each meniscus. The conservation of mass is thus

$$\frac{dV^*}{dt^*} = \pi[R^{*2} - (R^* - h_f^*)^2]U_f^* - \pi[R^{*2} - (R^* - h_r^*)^2]U_r^*. \tag{31}$$

Here U_f^* is the z component of velocity at the front meniscus tip and U_r^* is the z component of velocity at the rear meniscus tip. Equation (27) can be used to estimate h_r^*. The plug position Z_P^* is at the middle of the plug and is determined from the average of the front and rear meniscus-tip velocities as

$$\frac{dZ_P^*}{dt^*} = \frac{1}{2}(U_f^* + U_r^*). \tag{32}$$

Equations (30)–(32) were solved using an ordinary differential equation (ODE) solver from [51] (a PYTHON package). Inertia in the system is represented by the Laplace number $\lambda = \rho^*\sigma^*R^*/\mu^{*2}$,

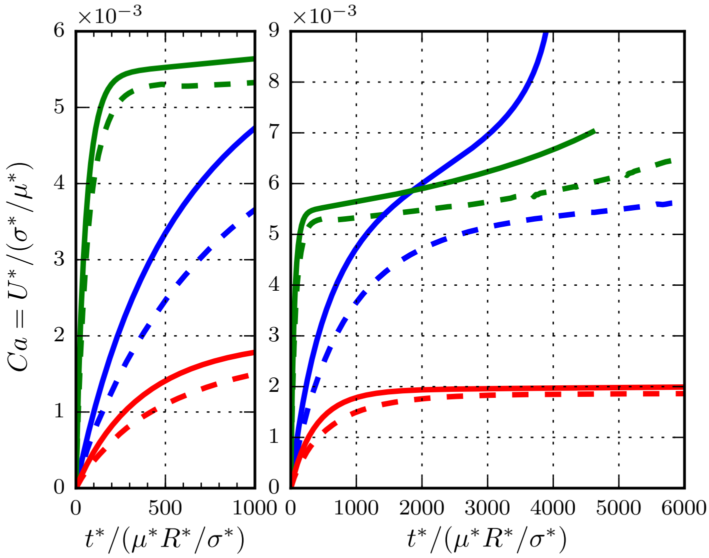

(a)

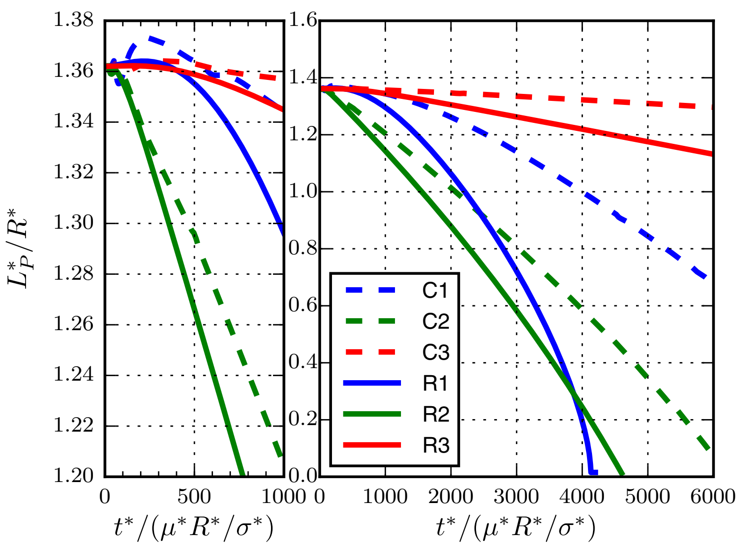

(b)

FIG. 8. The change in (a) the plug speed and (b) the plug length with time during the propagation of a liquid plug by a constant pressure drop $\Delta P = \Delta P^*/(\sigma^*/R^*)$. Here $C1$, $C2$, and $C3$ are CFD results, while $R1$, $R2$, and $R3$ are the reduced-dimension model results. The initial dimensionless plug length is $L^*_{P0}/R^* = 1.362$. The other parameters are $\Delta P = 0.34$, $h_f = 0.02$, and $\lambda = 22050$ for $C1$ and $R1$; $\Delta P = 0.34$, $h_f = 0.02$, and $\lambda = 2205$ for $C2$ and $R2$; and $\Delta P = 0.17$, $h_f = 0.01$, and $\lambda = 22\,050$ for $C3$ and $R3$.

which appears in the dimensionless form of Eq. (30) presented in Eq. (B1). For more detailed information, see Appendix B.

Figure 8 compares the evolution of the plug speed and the plug length between the CFD results ($C1$, $C2$, and $C3$) and the reduced-dimension model (RDM) results ($R1$, $R2$, and $R3$) for three combinations of $\Delta P = \Delta P^*/(\sigma^*/R^*)$, h_f, and λ, where ΔP is the constant pressure drop across the plug and h_f is the precursor film thickness, which were prescribed.

At $t^* = 0$, a stationary plug begins to propagate due to a constant pressure drop. For all cases, the initial plug length $L^*_{P0}/R^* = 1.362$. For the RDM, the plug volume was approximated by $V^* = L^*_P \pi R^{*2}$. We consider three cases: (i) $\Delta P = 0.34$, $h_f = 0.02$, and $\lambda = 22050$ ($R1$ and $C1$); (ii) $\Delta P = 0.34$, $h_f = 0.02$, and $\lambda = 2205$ ($R2$ and $C2$); and (iii) $\Delta P = 0.17$, $h_f = 0.01$, $\lambda = 22\,050$ ($R3$ and $C3$).

As discussed earlier, the plug length L_P increases (decreases) with time if the trailing film thickness h_r is thinner (thicker) than the precursor film thickness h_f. Since h_f is prescribed, the plug-length behavior is determined by h_r, which changes according to Eq. (27), and is a function of Ca. For all cases in Fig. 8, L_P decreases with time because $h_r > h_f$.

The plug speeds behave in a similar fashion during the initial acceleration stage ($t < 1000$). Specifically, $C2$ and $R2$ agree well for both plug speed and length. Thereafter, the RDM results gradually deviate from those of the CFD model for both Ca and L_P. The simulations from the RDM continue to increase to a larger value than the CFD model. Since h_r is a function of Ca, a small discrepancy in Ca causes a difference in L_P between the CFD model and the RDM. The discrepancy in Ca between the two models increases since the resistance in the plug core is a function of L_P.

The dimensionless time period for these two plug models to propagate through a distance of typical airway length $Z^*_P = 8R^*$ are $t^*/(\mu^* R^*/\sigma^*) = 2212$, 1470, and 4800 for $C1$, $C2$, and $C3$ and 1846, 1404, and 4360 for $R1$, $R2$, and $R3$, respectively. The errors of the RDM to CFD are 17%, 4%, and 9%, the errors in Ca are 21%, 5%, and 6%, and the errors in L_P are 11%, 7%, and 8% for ($C1$ and $R1$), ($C2$ and $R2$), and ($C3$ and $R3$), respectively.

There are several reasons that may explain the discrepancy between the long-term behavior of the RDM and the CFD model. First, the RDM does not take into account the interaction between the two menisci; this deviation is most likely to be an issue when L_P becomes small. As the plug length becomes shorter, the interaction of two menisci becomes significant and the trailing film thickness becomes thinner [36]. Second, the CFD model solves the full Navier-Stokes equations and includes the effect of inertia, while the RDM calculations are based upon interface resistances that are derived from Stokes flow calculations. Inertia was included in the RDM calculations by incorporating the

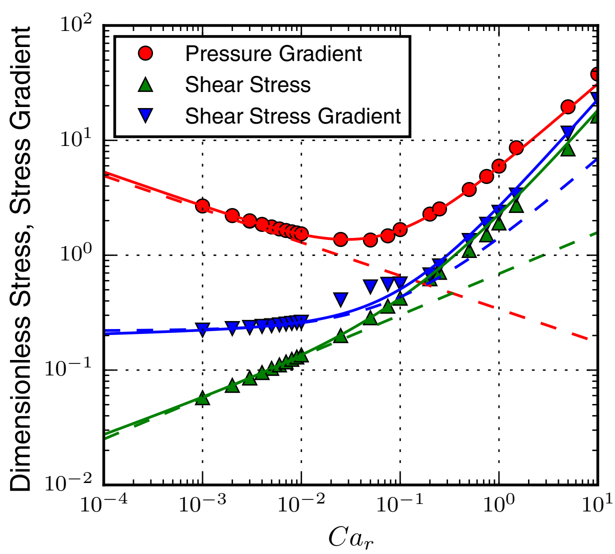

FIG. 9. Influence of Ca_r on the maximum wall mechanical stresses in the rear meniscus. The shear stress is scaled by σ^*/R^* and the pressure gradient and shear stress gradient are scaled by σ^*/R^{*2}. Symbols are computational results, solid lines are fitted curves ($r^2 = 0.969, 0.980, 0.903$), and dashed lines are fitted curves from [4].

TABLE III. Parameters of the mechanical stresses regression curve (33) with $x = \mathrm{Ca}_r$ for the rear meniscus.

$\tau_{\max}$	Pressure gradient	Shear stress	Shear stress gradient
k_1	5.57	1.78	0.265
k_2	0.337	0.498	2.40
n_1	0.744	0.987	0.0272
n_2	−0.299	0.315	0.971

change in mass of the system; however, the RDM calculations ignore convective acceleration effects that become important at higher velocities.

Finite-Reynolds-number effects not only change the flow fields in the plug core but also modify interface shapes [36]; the transition region of rear meniscus is longer and the capillary wave in front is more pronounced. This will cause higher resistance than Stokes flow. Evidently, $C2$ and $R2$ agree well, while the deviation in $C1$ and $R1$ is large because the Reynolds number $\mathrm{Re} = \lambda\mathrm{Ca}$ is much larger than $C2$ and $R2$. For all cases, the Ca for the RDM are larger than for the CFD model, which implies that the RDM underestimates the resistance. Despite these discrepancies, the simplified RDM calculations provide a faithful representation of plug dynamics that may be useful in large-scale models where full CFD calculations are untenable.

E. Wall mechanical stresses

The propagation of plugs in pulmonary airways is physiologically significant not only because it affects gas transfer, but also because it damages the epithelial cells due to the large pressure gradient that is induced by a moving meniscus [4,5]. Mechanical stresses can deform cells abnormally and may cause plasma membrane disruption and disrupt the tight junctions between epithelial cells [13]. This may cause leakage from the vascular system into the air spaces of the lung, which in turn may increase the liquid volume, deactivate the surfactant, and cause an exacerbation of ALI.

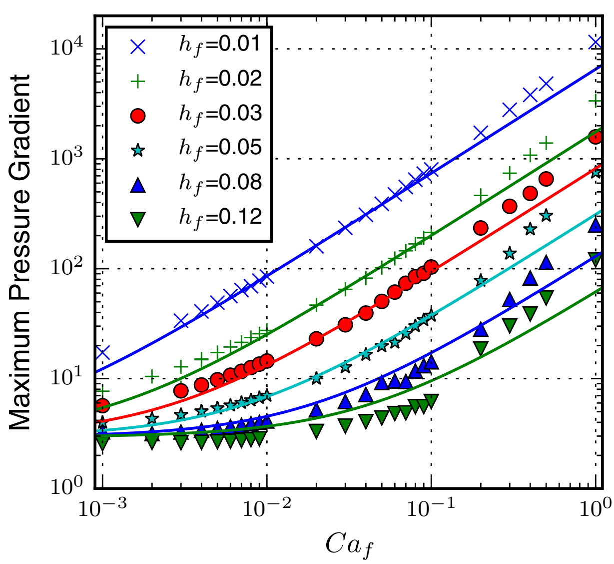

FIG. 10. Effects of Ca_f and the precursor film thickness h_f on the maximum wall pressure gradient in the front meniscus. Symbols are computational results and solid lines are fitted curves. Here $r^2 = 0.830$.

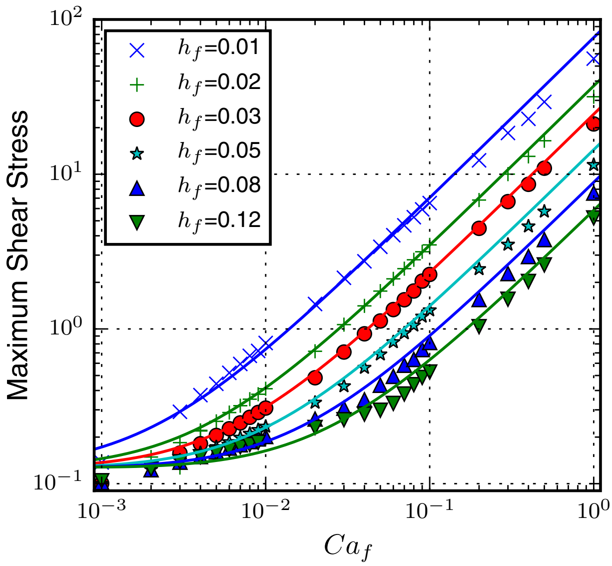

FIG. 11. Maximum wall shear stress in the front meniscus using the same parameters as in Fig. 10. Here $r^2 = 0.911$.

The maximum pressure gradient, the maximum shear stress, and the maximum shear stress gradient from the rear meniscus are plotted in Fig. 9 versus the capillary number Ca. Symbols are the computational results, while the solid lines are fitted curves of the form

$$\tau_{\max} = k_1 x^{n_1} + k_2 x^{n_2}, \tag{33}$$

where $x = \mathrm{Ca}_r$. The fitted parameters are listed in Table III. The dashed lines are fitted curves from Bilek *et al.* [4], which focused on small Ca. Experimental investigations showed that cell damage

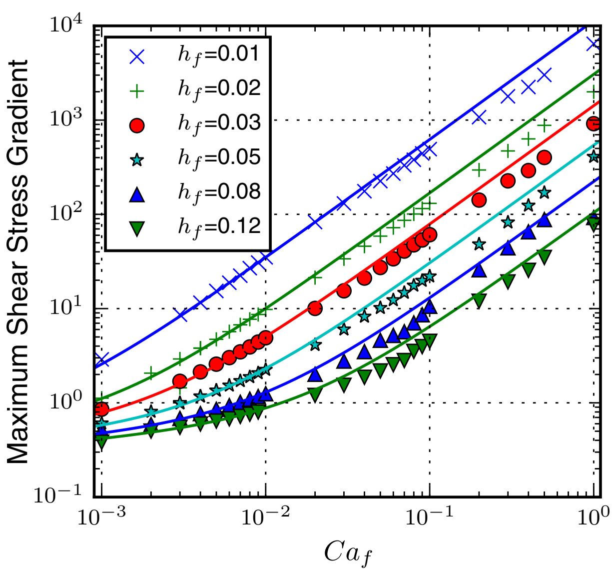

FIG. 12. Maximum wall shear stress gradient in the front meniscus. The values of h_f are the same as in Figs. 10 and 11. Here $r^2 = 0.511$.

TABLE IV. Parameters of the mechanical stresses regression curve (33) and $x = \mathrm{Ca}_f^m/h_f$ for the front meniscus.

$\tau_{\max}$	Pressure gradient	Shear stress	Shear stress gradient
m	1/2	1	2/3
k_1	1.05	0.633	0.716
k_2	2.93	0.107	1.86
n_1	1.90	1.04	0.233
n_2	0	−0.0299	1.89

increased with decreasing meniscus velocity [4,11,13]. This counterintuitive evidence correlates with the pressure gradient. The pressure gradient in Fig. 9 increased with decreasing Ca_r, where Ca_r decreases with the velocity at a fixed surface tension and viscosity. Therefore, in the rear meniscus, the pressure gradient is most likely the cause of cellular damage.

Figures 10–12 present, respectively, the maximum wall pressure gradient, shear stress, and shear stress gradient from the motion of the front meniscus. In contrast to the rear meniscus, these maximum mechanical stresses increase monotonically with Ca_f for each value of h_f. In addition, for a fixed Ca_f, they increase with a decrease of h_f. It should be noted that for small Ca_f, the magnitude of the stress and stress gradients is equivalent to that of the rear meniscus. Solid lines in Figs. 10–12 are fitted curves of Eq. (33) with $x = \mathrm{Ca}_f^m/h_f$. The fitted parameters are listed in Table IV, which may prove to be useful in large-scale RDM simulations.

V. CONCLUSION

In this study we have used computational models, from which we proposed simple but accurate semiempirical formulas for the flow resistance of a steadily propagating liquid plug in a liquid lined tube. These formulas were constructed by considering the plug flow resistance from three regional contributions: the front meniscus S_f, the plug core S_c, and the rear meniscus S_r.

We demonstrated that the nondimensional flow resistance of the front meniscus (S_f) is a function of Ca_f and h_f. For a fixed h_f, there is a peak in the S_f curve and S_f becomes negative when $h_f/(3\mathrm{Ca}_f)^{2/3} > 1$. We proposed Eq. (26) applied to Eq. (25) to estimate the flow resistance due to a moving front meniscus. The flow in the core region was modeled as Poiseuille flow, thus the flow resistance is a linear function of plug length, which is described by Eq. (11). This core model neglects interactions from the front and rear menisci and thus is more accurate for large plug lengths L_p. For the rear meniscus, the flow resistance increases monotonically with decreasing Ca_r. We proposed Eq. (29) to estimate the flow resistance due to the moving rear meniscus.

With the proposed resistance model, we simulated the propagation of plugs without performing expensive CFD analysis; this analysis was described in Sec. IV D and demonstrates excellent correlation for $t < 1000$. The behavior at larger times begins to deviate, likely due to convective inertia effects that are not incorporated in the RDMs. Nevertheless, RDMs provide the time for a plug to propagate an airway that deviates from full CFD simulations by less than 20% . When the Reynolds number is less than 50, the deviation is less than 10% .

Finally, we provided semiempirical formulas for the wall mechanical stresses at the front and rear menisci. These mechanical stresses have been correlated with cell injury from a propagating interface and may lead to atelectrauma that is associated with ventilation-induced lung injury [4–6,11,13]. We suggested that the general RDM approach can be easily applied to a large branching network system and may therefore be appropriate for creating predictive models of interfacial flow behavior in damaged pulmonary airways.

ACKNOWLEDGMENTS

This study was supported by National Science Foundation Grant No. CBET-1033619 and No. DMS-1043626. D.H. acknowledges the hospitality of the Biomedical Engineering Department during his sabbatical leave. Computational resources were supported in part using high performance computing resources and services provided by Technology Services at Tulane University.

APPENDIX A: FLOW RESISTANCE OF A PLUG

Bretherton [19] derived a model to describe the steady motion of a long Taylor bubble [18] using lubrication theory and showed that the pressure jump across the front meniscus of a bubble, which is equivalent to the rear meniscus of a liquid plug, is

$$\Delta P_r^* = [1 + 1.79(3\mathrm{Ca}_r)^{2/3}]\frac{2\sigma^*}{R^*}. \tag{A1}$$

where $\mathrm{Ca}_r = \mu^* U_r^*/\sigma^*$, with U_r^* the meniscus tip speed. Chebbi [48] extended Bretherton's analysis and showed that the pressure jump across the front meniscus of a long plug is

$$\Delta P_f^* = [1 + f_2(3\mathrm{Ca}_f)^{2/3}]\frac{2\sigma^*}{R^*}, \tag{A2}$$

where the function f_2 is related to the apparent contact angle. The latter is generated from the lubrication approximation and is given by Eq. (9), Here $\mathrm{Ca}_f = \mu^* U_f^*/\sigma^*$, with U_f^* the meniscus tip speed.

We assume that the plug core region can be described by Poiseuille flow. Then the pressure drop across the plug is

$$\Delta P^* = P_f^* - P_r^* = [-f_2(3\mathrm{Ca}_f)^{2/3} + 1.79(3\mathrm{Ca}_r)^{2/3}]\frac{2\sigma^*}{R^*} + \frac{8\mu^* L_P^* Q^*}{\pi R^{*4}}. \tag{A3}$$

Thus, the flow resistance of a plug defined by Eq. (17) is

$$S_{\mathrm{plug}}^* = [-f_2(3\mathrm{Ca}_f)^{2/3} + 1.79(3\mathrm{Ca}_r)^{2/3}]\frac{2\sigma^*}{\pi R^{*3} U^*} + \frac{8\mu^* L_P^*}{\pi R^{*4}}, \tag{A4}$$

where U^* is the cross-sectional averaged velocity. Scaling with $S_{\mathrm{plug}} = S_{\mathrm{plug}}^*/(\mu^*/\pi R^{*3})$ and $L_P = L_P^*/R^*$, the dimensionless flow resistance of a plug is

$$S_{\mathrm{plug}} = 2[-f_2(3\mathrm{Ca}_f)^{2/3} + 1.79(3\mathrm{Ca}_r)^{2/3}]\mathrm{Ca}^{-1} + 8L_P, \tag{A5}$$

where $\mathrm{Ca} = \sigma^* U^*/\mu^*$. With Eq. (19), Eq. (A5) for the total flow resistance is rewritten in terms of three contributions as

$$S_{\mathrm{plug}} = S_f + S_r + S_c, \tag{A6}$$

$$S_f = \hat{S}_f(1 - h_f)^{-2}, \tag{A7}$$

$$S_r = \hat{S}_r(1 - h_r)^{-2}, \tag{A8}$$

$$S_c = 8L_P, \tag{A9}$$

where

$$\hat{S}_f = -2 \times 3^{2/3} f_2 \mathrm{Ca}_f^{-1/3}, \tag{A10}$$

$$\hat{S}_r = 2 \times 1.79 \times 3^{2/3}\mathrm{Ca}_r^{-1/3}. \tag{A11}$$

For $\mathrm{Ca}_r \to 0$, $h_r \to 0$ and $S_r \to \hat{S}_r$. For $h_f \ll 1$ that is an assumption of the lubrication theory, $S_f \to \hat{S}_f$.

APPENDIX B: TRACKING A PLUG

This section provides details on how to utilize the plug resistance model to simulate plug propagation as presented in Sec. IV D. As above, using scaling of $\Delta P = \Delta P^*/(\sigma^*/R^*)$, $t = t^*/(\mu^* R^*/\sigma^*)$, $U = U^*/(\sigma^*/\mu^*)$, $L_P = L_P^*/R^*$, and $S_{\mathrm{plug}} = S_{\mathrm{plug}}^*/(\mu^*/\pi R^{*3})$ and assuming $V^* = L_P^* \pi R^{*2}$, the nondimensional form of Eqs. (30)–(32) can be combined into a system of ODEs

$$\frac{d}{dt}\begin{bmatrix} Z_P \\ U \\ L_P \end{bmatrix} = \begin{bmatrix} \frac{1}{2}(U_f + U_r) \\ \frac{1}{\lambda L_P}(\Delta P - S_{\mathrm{plug}} U) - \frac{U}{L_P}\frac{dL_P}{dt} \\ h_f(2-h_f)U_f - h_r(2-h_r)U_r \end{bmatrix}, \tag{B1}$$

where $\lambda = \rho^*\sigma^* R^*/\mu^{*2}$ is the Laplace number, Z_P is the middle of the plug and moves with the average of the front and rear meniscus tip velocities, where Eq. (19) can be used. To obtain h_r, Eq. (27) coupled with Eq. (19) needs to be solved. Since that is not easy, by applying $\mathrm{Ca}_r = \mathrm{Ca}$ for Eq. (27) and computing $\mathrm{Ca}_r = \mathrm{Ca}(1-h_r)^{-2}$, h_r is obtained with Eq. (27). With this approximation, the maximum error in h_r is 2.5%. Equation (B1) is of the form $y' = f(t,y)$, a system of explicit ODEs, which can be solved as an initial-value problem by standard ODE packages.

As an example, we consider a liquid plug with $\mu^* = 0.01$ P, $\rho^* = 1\ \mathrm{g/cm^3}$, and $\sigma^* = 25\ \mathrm{dyn/cm}$ that propagates in a tube of $R^* = 0.0882$ cm. Thus the Laplace number is $\lambda = 22\,050$. Initially, we assume that the plug is positioned at $z = 0$ with $U = 0$. We assume that the plug has formed from an unstable state where the dimensionless film thickness is $\epsilon = 0.12$ and that after the plug has been created the upstream and downstream film thicknesses are $h^*/R^* = h_f = 0.02$. Then the dimensionless plug length is $L_P = 1.362$ and the initial condition for Eq. (B1) is $y(0) = [0 \quad 0 \quad 1.362]^T$. We choose a driving pressure $\Delta P = 0.34$ that moves the plug in the z direction. Next we outline the algorithm used to compute plug motion.

To simulate plug motion, we must provide the function $f(t,y)$, which is the right-hand side of Eq. (B1) that the ODE solver calls many times as the evolution of y is being computed. The function $f(t,y)$ requires values of $U_f(t)$, $U_r(t)$, $U(t)$, $L_P(t)$ $S_{\mathrm{plug}}(t)$, $dL_P/dt(t)$, and $h_r(t)$ for a given $y(t) = [Z_P \quad U \quad L_P]^T$, while λ, ΔP, and h_f are known and constants. The trailing film thickness h_r can be computed by Eq. (27) coupled with Eq. (19) as described above. The resistance of plug S_{plug} is the sum of the resistances with contributions from the front meniscus S_f given by Eqs. (24)–(26) and (9), the rear meniscus S_r given by Eqs. (28) and (29), and the plug core region S_c given by Eq. (11). Since we scaled the velocity by σ^*/μ^*, $\mathrm{Ca} \equiv U_{\mathrm{tip}}$ and is thus given by Eq. (19). Further, dL_P/dt in the second component of $f(t,y)$ is determined by the third component of $f(t,y)$. This simulation provides the data presented in Fig. 8.

---

[1] P. T. Macklem, D. F. Proctor, and J. C. Hogg, The stability of peripheral airways, Respir. Physiol. **8**, 191 (1970).

[2] P. S. Hammond, Nonlinear adjustment of a thin annular film of viscous-fluid surrounding a thread of another within a circular cylindrical pipe, J. Fluid Mech. **137**, 363 (1983).

[3] P. A. Gauglitz and C. J. Radke, An extended evolution equation for liquid-film break up in cylindrical capillaries, Chem. Eng. Sci. **43**, 1457 (1988).

[4] A. M. Bilek, K. C. Dee, and D. P. Gaver, Mechanisms of surface-tension-induced epithelial cell damage in a model of pulmonary airway reopening, J. Appl. Physiol. **94**, 770 (2003).

[5] D. Huh, H. Fujioka, Y.-C. Tung, N. Futai, R. Paine, J. B. Grotberg, and S. Takayama, Acoustically detectable cellular-level lung injury induced by fluid mechanical stresses in microfluidic airway systems, Proc. Natl. Acad. Sci. USA **104**, 18886 (2007).

[6] H. W. Glindmeyer, B. J. Smith, and D. P. Gaver, In situ enhancement of pulmonary surfactant function using temporary flow reversal, J. Appl. Physiol. **112**, 149 (2012).
[7] D. P. Gaver, R. W. Samsel, and J. Solway, Effects of surface tension and viscosity on airway reopening, J. Appl. Physiol. **69**, 74 (1990).
[8] D. Dreyfuss and G. Saumon, Ventilator-induced lung injury: Lessons from experimental studies, Am. J. Respir. Crit. Care Med. **157**, 294 (1998).
[9] C. N. Sessler, G. L. Bloomfield, and A. A. Fowler, Current concepts of sepsis and acute lung injury, Clin. Chest Med. **17**, 213 (1996).
[10] A. S. Slutsky, Lung injury caused by mechanical ventilation, Chest **116**, 9S (1999).
[11] S. S. Kay, A. M. Bilek, K. C. Dee, and D. P. Gaver, Pressure gradient, not exposure duration, determines the extent of epithelial cell damage in a model of pulmonary airway reopening, J. Appl. Physiol. **97**, 269 (2004).
[12] H. L. Dailey, L. M. Ricles, H. C. Yalcin, and S. N. Ghadiali, Image-based finite element modeling of alveolar epithelial cell injury during airway reopening, J. Appl. Physiol. **106**, 221 (2009).
[13] A.-M. Jacob and D. P. Gaver, Atelectrauma disrupts pulmonary epithelial barrier integrity and alters the distribution of tight junction proteins ZO-1 and claudin 4, J. Appl. Physiol. **113**, 1377 (2012).
[14] C. Brun-Buisson, C. Minelli, G. Bertolini, L. Brazzi, J. Pimentel, K. Lewandowski, J. Bion, J. A. Rornand, J. Villar, A. Thorsteinsson, P. Damas, A. Armaganidis, and F. O. Lemaire, Epidemiology and outcome of acute lung injury in European intensive care units: Results from the ALIVE study, Intensive Care Med. **30**, 51 (2004).
[15] G. D. Rubenfeld, E. Caldwell, E. Peabody, J. Weaver, D. P. Martin, M. Neff, E. J. Stern, and L. D. Hudson, Incidence and outcomes of acute lung injury, New Engl. J. Med. **353**, 1685 (2005).
[16] L. B. Ware and M. A. Matthay, Medical progress: The acute respiratory distress syndrome, New Engl. J. Med. **342**, 1334 (2000).
[17] M. O. Maybauer, D. M. Maybauer, and D. N. Herndon, Incidence and outcomes of acute lung injury, New Engl. J. Med. **354**, 416 (2006).
[18] G. I. Taylor, Deposition of a viscous fluid on the wall of a tube, J. Fluid Mech. **10**, 161 (1961).
[19] F. P. Bretherton, The motion of long bubbles in tubes, J. Fluid Mech. **10**, 166 (1961).
[20] E. Klaseboer, R. Gupta, and R. Manica, An extended Bretherton model for long Taylor bubbles at moderate capillary numbers, Phys. Fluids **26**, 032107 (2014).
[21] P. Aussillous and D. Quere, Quick deposition of a fluid on the wall of a tube, Phys. Fluids **12**, 2367 (2000).
[22] B. G. Cox, On driving a viscus fluid out of a tube, J. Fluid Mech. **14**, 81 (1962).
[23] D. A. Reinelt and P. G. Saffman, The penetration of a finger into a viscous-fluid in a channel and tube, SIAM J. Sci. Stat. Comput. **6**, 542 (1985).
[24] D. Halpern and D. P. Gaver, Boundary-element analysis of the time-dependent motion of a semiinfinite bubble in a channel, J. Comput. Phys. **115**, 366 (1994).
[25] M. D. Giavedoni and F. A. Saita, The axisymmetric and plane cases of a gas phase steadily displacing a Newtonian liquid: A simultaneous solution of the governing equations, Phys. Fluids **9**, 2420 (1997).
[26] M. D. Giavedoni and F. A. Saita, The rear meniscus of a long bubble steadily displacing a Newtonian liquid in a capillary tube, Phys. Fluids **11**, 786 (1999).
[27] M. Heil, Finite Reynolds number effects in the Bretherton problem, Phys. Fluids **13**, 2517 (2001).
[28] G. M. Ginley and C. J. Radke, Influence of soluble surfactants on the flow of long bubbles through a cylindrical capillary, ACS Symp. Ser. **396**, 480 (1989).
[29] J. Ratulowski and H. C. Chang, Marangoni effects of trace impurities on the motion of long gas-bubbles in capillaries, J. Fluid Mech. **210**, 303 (1990).
[30] C. W. Park, Influence of soluble surfactants on the motion of a finite bubble in a capillary-tube, Phys. Fluids A **4**, 2335 (1992).
[31] F. Wassmuth, W. G. Laidlaw, and D. A. Coombe, Calculation of interfacial flows and surfactant redistribution as a gas-liquid interface moves between 2 parallel plates, Phys. Fluids A **5**, 1533 (1993).
[32] K. J. Stebe and D. Barthes-Biesel, Marangoni effects of adsorption-desorption controlled surfactants on the leading end of an infinitely long bubble in a capillary, J. Fluid Mech. **286**, 25 (1995).

[33] S. N. Ghadiali and D. P. Gaver, The influence of non-equilibrium surfactant dynamics on the flow of a semi-infinite bubble in a rigid cylindrical capillary tube, J. Fluid Mech. **478**, 165 (2003).
[34] P. D. Howell, S. L. Waters, and J. B. Grotberg, The propagation of a liquid bolus along a liquid-lined flexible tube, J. Fluid Mech. **406**, 309 (2000).
[35] S. L. Waters and J. B. Grotberg, The propagation of a surfactant laden liquid plug in a capillary tube, Phys. Fluids **14**, 471 (2002).
[36] H. Fujioka and J. B. Grotberg, Steady propagation of a liquid plug in a two-dimensional channel, J. Biomech. Eng. **126**, 567 (2004).
[37] H. Fujioka and J. B. Grotberg, The steady propagation of a surfactant-laden liquid plug in a two-dimensional channel, Phys. Fluids **17**, 082102 (2005).
[38] Y. Zheng, H. Fujioka, and J. B. Grotberg, Effects of gravity, inertia, and surfactant on steady plug propagation in a two-dimensional channel, Phys. Fluids **19**, 082107 (2007).
[39] D. M. Campana, S. Ubal, M. D. Giavdoni, and F. A. Saita, Stability of the steady motion of a liquid plug in a capillary tube, Ind. Eng. Chem. Res. **46**, 1803 (2007).
[40] H. Fujioka, S. Takayama, and J. B. Grotberg, Unsteady propagation of a liquid plug in a liquid-lined straight tube, Phys. Fluids **20**, 062104 (2008).
[41] E. A. Hassan, E. Uzgoren, H. Fujioka, J. B. Grotberg, and W. Shyy, Adaptive Lagrangian-Eulerian computation of propagation and rupture of a liquid plug in a tube, Int. J. Numer. Methods Fluids **67**, 1373 (2011).
[42] V. Suresh and J. B. Grotberg, The effect of gravity on liquid plug propagation in a two-dimensional channel, Phys. Fluids **17**, 031507 (2005).
[43] P. Zamankhan, B. T. Helenbrook, S. Takayama, and J. B. Grotberg, Steady motion of Bingham liquid plugs in two-dimensional channels, J. Fluid Mech. **705**, 258 (2012).
[44] Y. Zheng, J. C. Anderson, V. Suresh, and J. B. Grotberg, Effect of gravity on liquid plug transport through an airway bifurcation model, J. Biomech. Eng. **127**, 798 (2005).
[45] Y. Zheng, H. Fujioka, J. C. Grotberg, and J. B. Grotberg, Effects of inertia and gravity on liquid plug splitting at a bifurcation, J. Biomech. Eng. **128**, 707 (2006).
[46] B. J. Smith and D. P. Gaver, Agent-based simulations of complex droplet pattern formation in a two-branch microfluidic network, Lab Chip **10**, 303 (2010).
[47] M. Filoche, C.-F. Tai, and J. B. Grotberg, Three-dimensional model of surfactant replacement therapy, Proc. Natl. Acad. Sci. USA **112**, 9287 (2015).
[48] R Chebbi, Deformation of advancing gas-liquid interfaces in capillary tubes, J. Colloid Interface Sci. **265**, 166 (2003).
[49] S. Kalliadasis and H. C. Chang, Apparent dynamic contact angle of an advancing gas–liquid meniscus, Phys. Fluids **6**, 12 (1994).
[50] M. J. Martinez and K. S. Udell, Boundary integral analysis of the creeping flow of long bubbles in capillaries, J. Appl. Mech. **56**, 211 (1989).
[51] E. Jones, T. Oliphant, P. Peterson *et al.*, SciPy: Open source scientific tools for PYTHON (2001–), available at scipy.org